Equivalent Circuit Modeling of *LLC* Resonant Converter

Shuilin Tian, Fred C. Lee, *Life Fellow, IEEE*, and Qiang Li, *Member, IEEE*

***Abstract*—*LLC* resonant converter is widely used in industry. However, up to now, no simple and accurate small-signal equivalent circuit model is available. This article proposes an equivalent circuit model of *LLC* resonant converter. The simple equivalent circuit model is derived based on modification and simplification of extended describing function method, which has already been successful deriving equivalent circuit model in series resonant converter [15]. The model can well predict the small-signal behaviors observed in pulse-frequency-modulated *LLC* resonant converter, whenever switching frequency is below, close to, or above the resonant frequency. For the first time, analytical expressions for control to output voltage, input to output voltage, input impedance, and output impedance are provided to aid closed-loop feedback design. SIMPLIS simulation and experimental results are presented to prove the accuracy of the model.**

***Index Terms*—DC-DC converter, equivalent circuit, *LLC* resonant converter, modeling.**

I. Introduction

DC–DC converters, in general, can be divided into two categories: pulsewidth modulation (PWM) converters, and resonant converters. As most of the applications involve a regulated output voltage, a feedback loop is incorporated into the control system to stabilize the output voltage. For optimal design purpose, small-signal equivalent circuit models are indispensable. For PWM converters, equivalent circuit models are available to engineers for most of the control methods. First, for single loop (voltage mode) control, averaging concept is widely used. This concept was first proposed by Wester and Middlebrook [1] and then represented in state-space approach by Middlebrook and Cuk [2]. To provide more insights on circuit level, three-terminal switch model was proposed by Tymerski *et al.* [3] and Vorperian [4]. Second, for current mode control, the inductor current has sideband effect and it causes subharmonic problem in some cases ($D > 0.5$ for peak current mode) [5]. In this case, average concept breaks down as the switching frequency components are neglected. A more advanced modeling methodology describing function method is successfully applied to all kinds of current mode controls by Li and Lee [5] and analytical transfer functions are derived. To provide more physical insights, unified three-terminal switch models are developed by Yan *et al.* [6] and Tian *et al.* [7]. Third, for V^2 control or ripple-based control methods, both the capacitor voltage and inductor current have the sideband effects [11]. Analytical small-signal models are derived based on describing function method by Li and Lee [8] and further analyzed by Tian *et al.* [9], [10]. To provide more physical insights, a unified equivalent circuit model for V^2 control is developed in [11] and optimal design guidelines are proposed for point-of-load applications employing ceramic caps. Therefore, for PWM converters, feedback design is straightforward with the help of all these research efforts.

However, compared with PWM converters, the scenario is more complex for resonant converters. Even for the simplest resonant converter: series resonant converter (SRC), the averaging concept breaks down. The reason is that for resonant converters, some of the state variables do not have dc components but contain strong switching frequency component and its harmonics, whereas the dc components are the dominant parts of the state variables for PWM converters. Due to the strong oscillatory nature of resonant states, the switching frequency interacts with the natural resonant frequency. This results in an interesting phenomenon, which is often referred to as the beat frequency dynamics where the high-frequency response is determined by a pair of double pole located at the beat frequency [12]. The beat frequency dynamics cannot be investigated using the averaging concept because it eliminates the switching frequency information. Up to today, the most successful model to predict the beat frequency dynamics is based on extended describing function method by Yang *et al.* [13]. This method utilizes the multivariable describing functions to treat the system nonlinearities. This method provides continuous time small-signal models in state-space representation, which can include any number of harmonics for good model accuracy. An equivalent circuit model is proposed for simulation purpose, taking only the fundamental components to represent the tank variables. The equivalent circuit model is cross-coupled and very complex. Recently, a decent simple third-order equivalent circuit model is developed by Tian *et al.* [14], [15] to explain all the small-signal properties, including the beat frequency dynamics, in SRC. Besides, for the first time, analytical expressions of all transfer functions are presented for closed-loop feedback design of SRC.

Manuscript received July 8, 2019; revised October 1, 2019 and December 7, 2019; accepted January 13, 2020. Date of publication January 16, 2020; date of current version April 22, 2020. This work was supported by the PMC Consortium in Center for Power Electronics System, Virginia Tech. This paper was presented in part at the IEEE Applied Power Electronics Conference and Exposition, Long Beach, CA, USA, March 2016. Recommended for publication by Associate Editor H. S. Krishnamoorthy. *(Corresponding author: Shuilin Tian.)*

S. Tian is with the Analog Device. Inc., Santa Clara, CA 95054, USA (e-mail: tianshuilinpe@gmail.com).

F. C. Lee and Q. Li are with the Center for Power Electronics Systems, Virginia Tech, Blacksburg, VA 24061 USA (e-mail: fclee@vt.edu; lqvt@vt.edu).

Color versions of one or more of the figures in this article are available online at https://ieeexplore.ieee.org.

Digital Object Identifier 10.1109/TPEL.2020.2967346

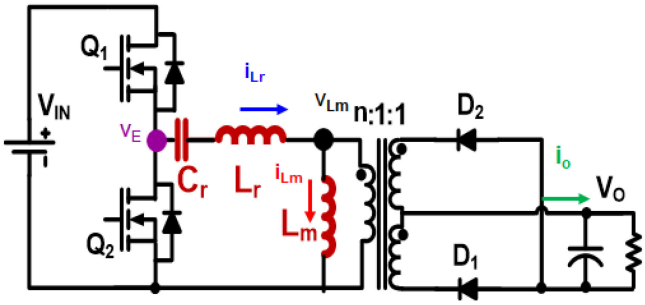

Fig. 1. Schematic of half-bridge *LLC* resonant converter (*LLC*).

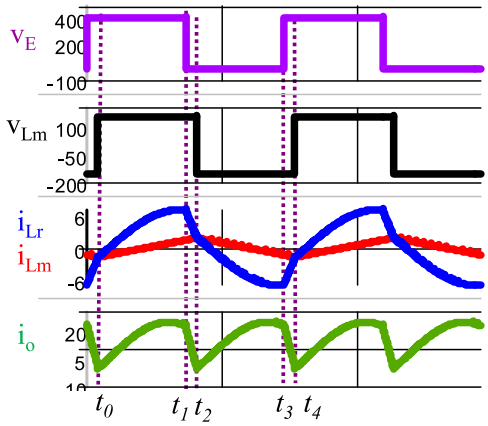

Fig. 2 Steady-state waveforms for $F_s = 1.4F_o$.

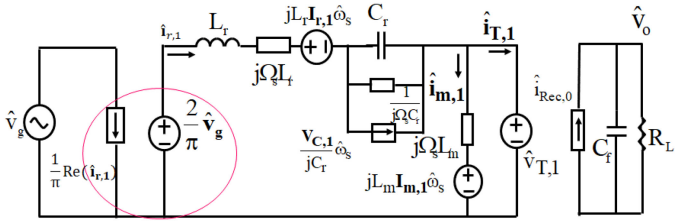

Fig. 3. Small-signal model of *LLC* for $F_s \geq F_o$.

LLC resonant converter, shown as Fig. 1 (with half-bridge form), is the most popular resonant converter for front-end dc–dc converters used in distributed power systems in telecom, computer, and network applications [16], [17]. Besides, they are also widely adopted in other applications, such as LCD, LED, and plasma display in TV and flat panels; iron implanter arc power supply; solar array simulator in photovoltaic application; fuel cell applications, and so on. Available small-signal models published in literatures include extended describing function method [18]–[21], approach based on communication theory [22], sampled-data modeling approach [23], analysis based on SIMPLIS simulation [24], or bench measurement results [25]. All of the above models use numerical solutions instead of analytical solutions. As a result, no simple equivalent circuit model is available, and no analytical expressions of transfer functions are presented.

This article proposes a simple equivalent circuit model as a good design tool for *LLC* resonant converter. The simple equivalent circuit model is derived based on and simplification of extended describing function method, following similar strategy on SRC resonant converter [14], [15], with some necessary modification for the case when switching frequency F_s is below resonant frequency F_o. The following two main objectives will be achieved. 1) A simple third-order equivalent circuit model of *LLC* resonant converter is proposed. The equivalent circuit model can well predict beat frequency dynamics and provide fruitful physical insights to understand the small-signal behavior. 2) For the first time, analytical expressions for all transfer functions are provided to help engineers to design the feedback control appropriately. This article is an extension of the conference paper [27], with the addition of more experimental results, a session discussing the model limits and accuracy (see Section IV-C), and more material for the model derivation process. The remaining article is organized as follows. The unified third-order equivalent circuit model is developed and proposed in Section II. Section III discusses two important aspects about the small-signal behavior with the proposed equivalent circuit: dc gain and beat frequency dynamics. Besides, analytical expressions of all transfer functions are presented for easy reference. Section IV provides SIMPLIS simulation and experimental results to verify the proposed equivalent circuit model. Besides, the model accuracy and limits are discussed. Finally, Section V concludes this article.

II. Equivalent Circuit Model of *LLC* Resonant Converter

For *LLC* resonant converter, one major advantage is its zero-voltage switching (ZVS) capability for zero to full load range. Generally speaking, ZVS is preferred for applications using MOSFET. For SRC, ZVS can only be achieved when switching frequency is above the resonant frequency. However, for *LLC*, due to the effect of L_m, ZVS can also be achieved when switching frequency is below the series resonant frequency F_o. From resonance point of view, the resonant tank is different when comparing $F_s \geq F_o$ with $F_s \leq F_o$. For $F_s \geq F_o$, only L_r resonates with C_r and L_m is always clamped by the output voltage. For $F_s < F_o$, there is a certain time period that L_m also participates in resonance. Due to different resonant behaviors, the small-signal models are developed for each case, as follows.

A. *Equivalent Circuit Model of* LLC *for* $F_s \geq F_o$

As shown in steady-state waveform in Fig. 2, in this case, *LLC* behaves like SRC. The magnetizing inductor L_m is either clamped by V_o or $-V_o$ and never participates in resonance.

The model of inverter, rectifier, resonant inductor, and resonant capacitor can be derived following the same methodology as SRC, shown in [15]. During the derivation, fundamental approximation is used, i.e., only fundamental components of the resonant tank variable are considered. Fig. 3 shows the small-signal model of *LLC* resonant converter for $F_s \geq F_o$. Note that since half-bridge inverter is used in *LLC* resonant converter, compared with the full-bridge inverter model, shown in [15], the

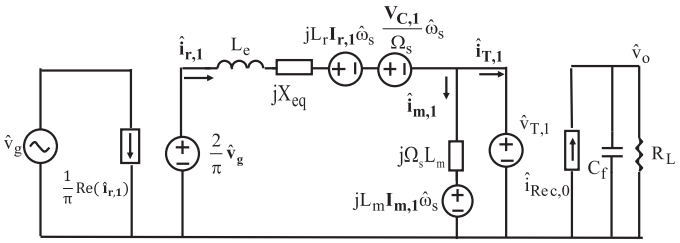

Fig. 4. Small-signal model of *LLC* for $F_s \geq F_o$ with simplified resonant capacitor branch.

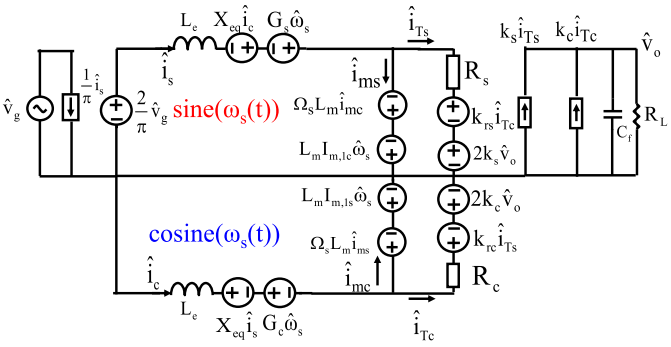

Fig. 5. Separated third-order equivalent circuit model of *LLC* for $F_s \geq F_o$.

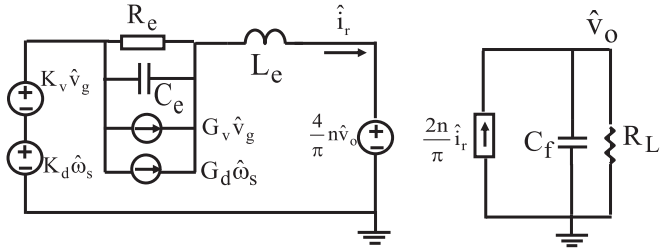

Fig. 6. Noncoupled third-order equivalent circuit model of *LLC* for $F_s \geq F_o$.

magnitude of the current source and voltage source is reduced to half on the inverter side (shown in red circle).

Similar as SRC [15], the resonant capacitor behaves like an equivalent inductor with respect to modulation frequency.

This phenomenon is very interesting as it is somewhat against the common sense in the PWM converter. The capacitor and the inductor are the two basic energy storage elements with very different dynamic behavior. However, with the formal mathematical derivation shown in [15], in the resonant converter, for low-frequency modulation signal, the capacitor behaves like an equivalent inductor with respect to the modulation frequency. It should be noted that this conclusion is only valid in the case that the modulation signal is carried by the carrier frequency (switching frequency). Therefore, this phenomenon only exists in resonant converters and can never be observed in PWM-type converters.

Therefore, the resonant tank can be simplified, as shown in Fig. 4.

In this article, F (in Hz) is the frequency, whereas Ω is the angular frequency (in radians/s). Angular frequency Ω is larger than frequency F by a factor of 2π. For examples, $\Omega_s = 2\pi F_s$ and $\Omega_o = 2\pi F_o$. The expression of equivalent inductor L_e and impedance X_{eq} is shown as follows:

$$L_e = L_r + \frac{1}{C_r\Omega_s^2} = L_r\left(1+\frac{\Omega_o^2}{\Omega_s^2}\right)$$
$$X_{\mathrm{eq}} = \Omega_s L_r - \frac{1}{\Omega_s C_r}. \tag{1}$$

The small-signal model shown in Fig. 4 has complex terms and cannot be used for simulation. Following the similar methodology as SRC [15], the complex terms can be eliminated by separating the resonant tank into sine part and cosine part, shown as Fig. 5.

Similar as SRC [15], the superposition theorem is applied to derive a noncoupled equivalent circuit model. The noncoupled equivalent circuit is shown as Fig. 6.

L_e, R_e, and C_e are used to represent beat frequency dynamics and their expressions are same as SRC. L_e and C_e determine the location of the double pole and R_e provides the damping of the double pole. The expressions of K_v, G_v, K_d, and G_d are different from SRC and will be affected by the design of L_m. All the expressions are shown as follows:

$$L_e = L_r\left(1+\frac{\Omega_o^2}{\Omega_s^2}\right), C_e = \frac{1}{L_e(\Omega_s-\Omega_o)^2}$$

$$R_e = \frac{L_e\,|X_{\mathrm{eq}}|\,|\Omega_s-\Omega_o|}{R_{\mathrm{eq}}}$$

$$G_d = \frac{2V_g}{\pi}\frac{L_n}{\Omega_0}\frac{1}{R_e}$$

$$\left(\frac{\frac{1}{\Omega_n}\left(\frac{1}{\Omega_n^2}-\Omega_n^2\right)\left(\frac{\pi^2}{8}QL_n\right)^2-\left(L_n+1-\frac{1}{\Omega_n^2}\right)\left(\frac{2}{\Omega_n^3}\right)}{\left[\sqrt{\left(L_n+1-\frac{1}{\Omega_n^2}\right)^2+\left(\left(\frac{1}{\Omega_n}-\Omega_n\right)\frac{\pi^2}{8}QL_n\right)^2}\right]^2}+\frac{2}{L_n^2}\right)$$

$$K_d = -\frac{4V_g}{\pi}\frac{1}{\Omega_o L_n}, G_v = \frac{1}{\pi}\frac{X_{\mathrm{eq}}}{\sqrt{X_{\mathrm{eq}}^2+R_{\mathrm{eq}}^2}}$$

$$K_v = \frac{4}{\pi^2}\frac{V_g L_n \Omega_n}{R_{\mathrm{eq}}}\frac{L_n+1-\frac{1}{\Omega_n^2}}{\sqrt{\left(L_n+1-\frac{1}{\Omega_n^2}\right)^2+\left(\left(\frac{1}{\Omega_n}-\Omega_n\right)\frac{\pi^2}{8}QL_n\right)^2}}$$

$$R_{\mathrm{eq}} = \frac{8}{\pi^2}n^2R_L, X_{\mathrm{eq}} = \Omega_s L_r - \frac{1}{\Omega_s C_r}, L_n = \frac{L_m}{L_r}$$

$$\Omega_n = \frac{\Omega_s}{\Omega_o}, Q = \frac{\sqrt{L_r/C_r}}{n^2\cdot R_L}. \tag{2}$$

B. Equivalent Circuit Model of LLC *for* $F_s < F_o$

Fig. 7 shows the steady-state waveforms when $F_s = 0.8F_o$, and Fig. 8 shows the operating modes at different time periods. Obviously, in this case, the resonant tank changes at different time periods; in time periods [t_0, t_1] and [t_2, t_3], the magnetizing inductor L_m is either clamped by V_o or –V_o and never participates in resonance. This is exactly the same condition as

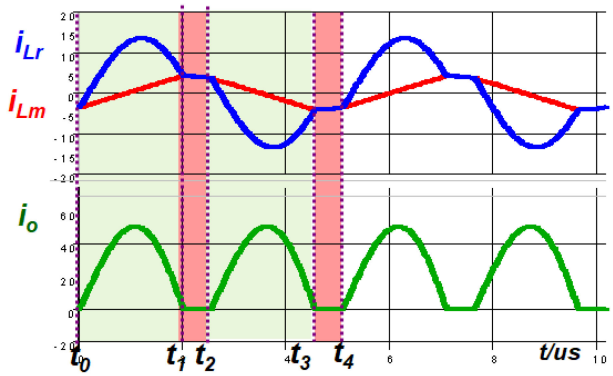

Fig. 7. Steady-state waveforms for $F_s = 0.8F_o$.

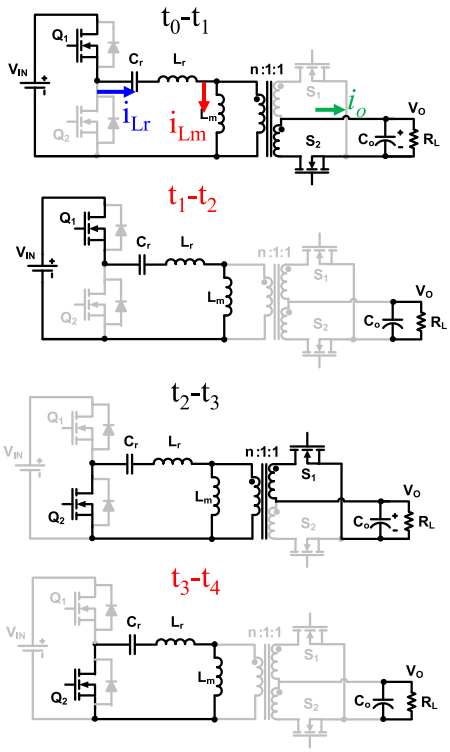

Fig. 8. Operating modes of *LLC* for $F_s < F_o$.

previous case when $F_s \geq F_o$; in time periods $[t_1, t_2]$ and $[t_3, t_4]$, the magnetizing inductor L_m participates in resonance and the resonant tank is comprised of C_r and L_r in series with L_m. In the meanwhile, the output load is decoupled from the resonant tank. As the resonant tank is changing within one switching period, the *LLC* essentially belongs to multiresonant structure when operating in the region $F_s < F_o$.

In time periods $[t_0, t_1]$ and $[t_2, t_3]$, tank and load are coupled and the relation of L_m, rectifier, and output load are same as $F_s \geq F_o$ case, as shown in Fig. 9(a). In time periods $[t_1, t_2]$ and $[t_3, t_4]$, tank and load are decoupled. In this case, L_r is in series with L_m and the sum of the two inductances resonates with C_r, as shown in Fig. 9(b).

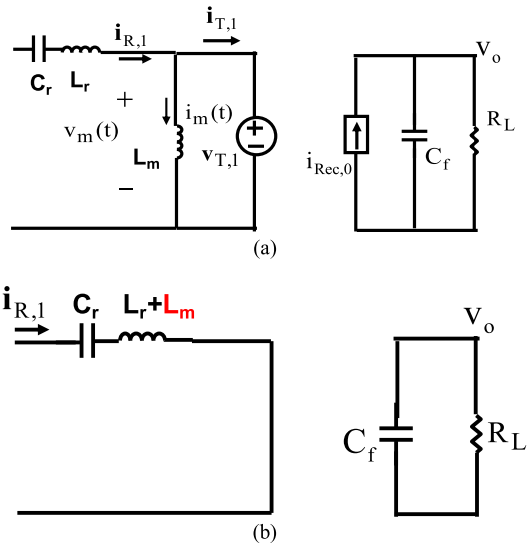

Fig. 9. Relation of L_m, rectifier, and output load for $F_s < F_o$. (a) In time periods $[t_0, t_1]$ and $[t_2, t_3]$. (b) In time periods $[t_1, t_2]$ and $[t_3, t_4]$.

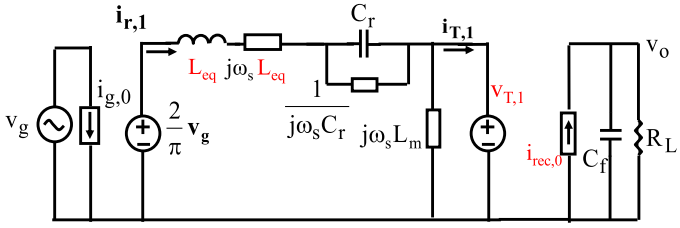

Fig. 10. Large-signal modulation model of *LLC* for $F_s < F_o$.

The length of time periods $[t_0, t_1]$ and $[t_2, t_3]$ is the resonant period T_o and the length of time periods $[t_1, t_2]$ and $[t_3, t_4]$ is $T_s - T_o$. For the whole switching period, the modulation model can be derived by combining the modulation model of Fig. 9(a) and (b), with the ratio of T_o/T_s and $(T_s - T_o)/T_s$, respectively. The large-signal modulation model is shown as Fig. 10.

The equivalent resonant inductor L_{eq} is related with resonant inductor and magnetizing inductor. The expression of L_{eq} is shown as follows:

$$L_{\text{eq}} = L_r \frac{T_o}{T_s} + (L_r + L_m) \frac{(T_s - T_o)}{T_s} = L_r + L_m \frac{\Omega_o - \Omega_s}{\Omega_o}. \tag{3}$$

For $F_s < F_o$, the model of the rectifier should be modified, as the voltage across the magnetizing inductor is a quasi-square-wave instead of a square wave, as shown in Fig. 11(b).

The modulation model and small-signal model are shown in Fig. 12 and the expressions are shown in (4). When $F_s = F_o$, the quasi-square-wave of V_T becomes square wave and the model of the rectifier reduces to the model used in SRC.

With the modified modulation model and small-signal model of the rectifier, the small-signal model of *LLC* for $F_s < F_o$ can be derived, shown as Fig. 13

$$v_{T,1} = \frac{4}{\pi} n v_o \sin\left(\frac{1}{2}\frac{\Omega_s}{\Omega_o}\pi\right) \frac{i_{T,1}}{\|i_{T,1}\|}$$

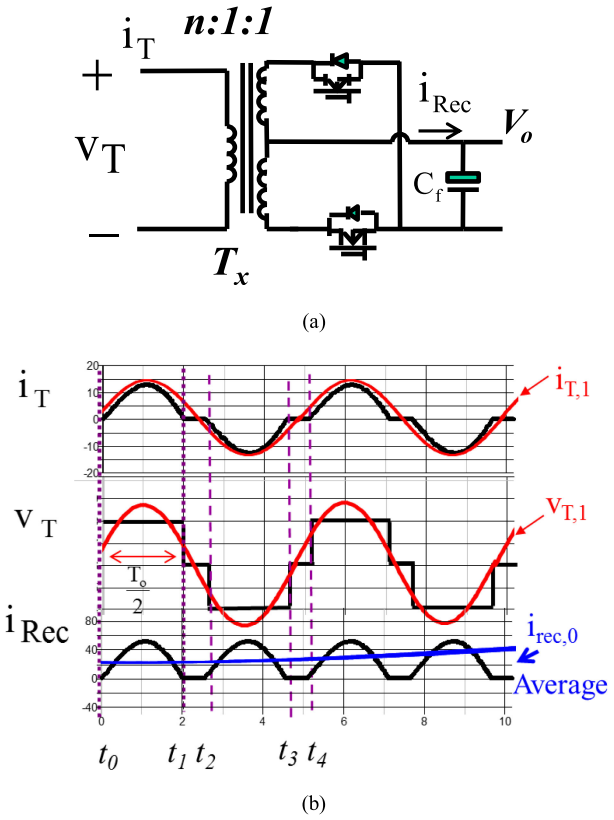

Fig. 11 (a) Structure. (b) Waveforms of the rectifier of *LLC* for $F_s < F_o$.

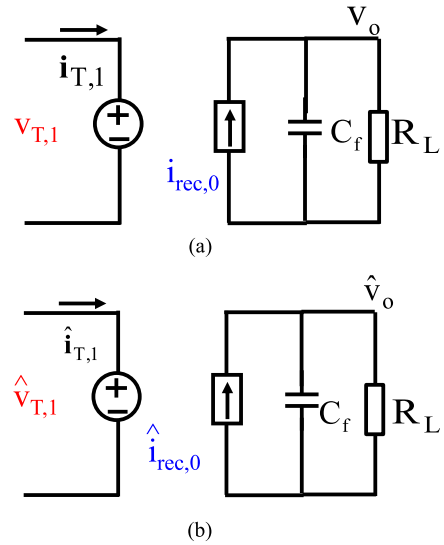

Fig. 12. (a) Modulation model. (b) Small-signal model of the rectifier of *LLC* for $F_s < F_o$.

$$
\begin{aligned}
i_{rec,0} &= \frac{2}{\pi}\|ni_{T,1}\| \\
\hat{v}_{T,1} &= \sin\left(\frac{1}{2}\frac{\Omega_s}{\Omega_o}\pi\right)\left(k_{vo}\hat{v}_o + k_{is}\hat{i}_{T,s} + k_{ic}\hat{i}_{T,c}\right) \\
\hat{i}_{rec,0} &= k_s\hat{i}_{T,s} + k_c\hat{i}_{T,c}.
\end{aligned} \tag{4}
$$

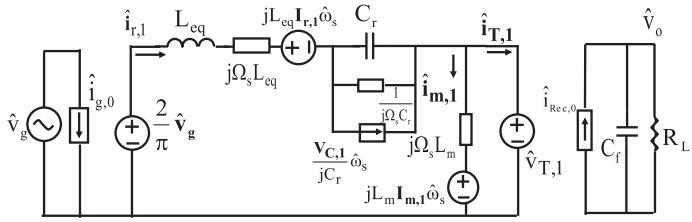

Fig. 13. Small-signal model of *LLC* for $F_s < F_o$.

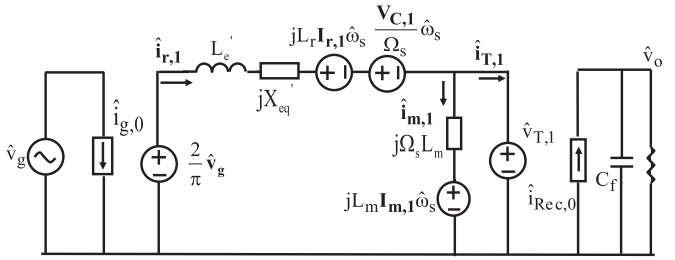

Fig. 14. Small-signal model of *LLC* for $F_s < F_o$ with simplified resonant capacitor branch.

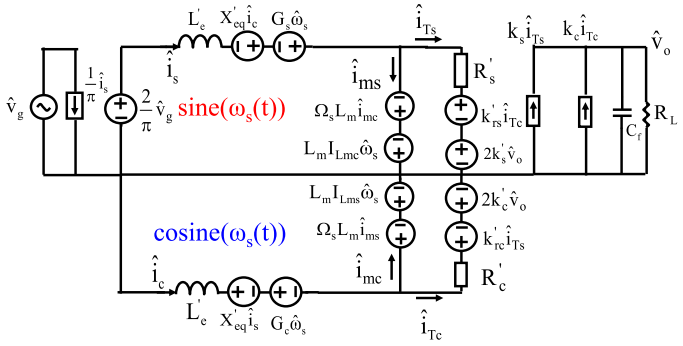

Fig. 15. Separated equivalent circuit model of *LLC* for $F_s < F_o$.

Similar to the previous case in SRC [15], the resonant capacitor behaves like an equivalent inductor with respect to modulation frequency. Therefore, the resonant tank can be simplified as shown in Fig. 14.

The expressions of equivalent inductor L_e' and impedance X_{eq}' are modified by L_m and shown as follows:

$$
\begin{aligned}
\mathbf{L'_e} &= \mathbf{L_r} + \mathbf{L_m}\frac{\Omega_o - \Omega_s}{\Omega_o} + \frac{1}{C_r\Omega_s^2} = \mathbf{L_r}\left(\mathbf{1} + \frac{1}{\Omega_n^2}\right) \\
&\quad + \mathbf{L_m}\left(\mathbf{1} - \mathbf{\Omega_n}\right), \ \textbf{where} \ \ \mathbf{\Omega_n} = \frac{\mathbf{\Omega_s}}{\mathbf{\Omega_o}} \\
\mathbf{X'_{eq}} &= \mathbf{\Omega_s}\left(\mathbf{L_r} + \mathbf{L_m}\left(\mathbf{1} - \mathbf{\Omega_n}\right)\right) - \frac{\mathbf{1}}{\mathbf{\Omega_s C_r}}.
\end{aligned} \tag{5}
$$

Following the similar methodology as previous case in SRC [15], the complex terms can be eliminated by separating the resonant tank into sine part and cosine part, shown as Fig. 15.

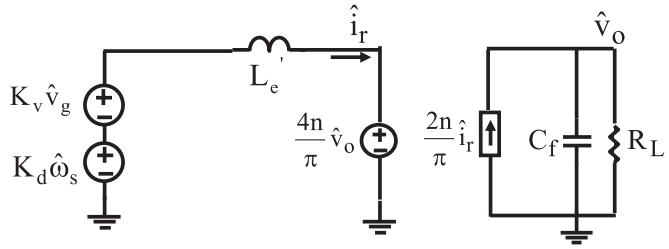

Fig. 16. Noncoupled equivalent circuit model of *LLC* for $F_s < F_o$.

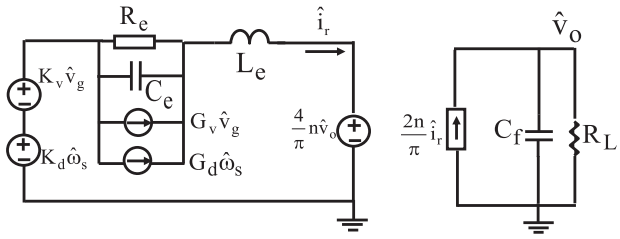

Fig. 17. Unified equivalent circuit model of *LLC*.

The expressions of the new parameters related with modified rectifier are shown as follows:

$$\mathbf{R'_s = R_s\ sin\left(\frac{\pi}{2}\Omega_n\right)}, \mathbf{R'_c = R_c\ sin\left(\frac{\pi}{2}\Omega_n\right)}$$
$$\mathbf{k'_{rs} = k'_{rc} = k_{rs}\ sin\left(\frac{\pi}{2}\Omega_n\right)}$$
$$\mathbf{k'_s = k_s\ sin\left(\frac{\pi}{2}\Omega_n\right)}, \mathbf{k'_c = k_c\ sin\left(\frac{\pi}{2}\Omega_n\right)}. \quad (6)$$

Similar as previous case, the superposition theorem is applied to derive a noncoupled equivalent circuit model. The detailed derivation process is similar as SRC case, which is listed in [15, Appendix]. The noncoupled equivalent circuit is shown as Fig. 16. The expressions of L'_e, K_v, and K_d are shown as follows:

$$L'_e = L_r\left(1+\frac{1}{\Omega_n^2}\right) + L_m\left(1-\Omega_n\right)$$

$$K_d = \frac{2V_g}{\pi}\frac{L_n}{\Omega_o}$$
$$\left[\frac{\left[\left(\frac{1}{\Omega_n^2}-\Omega_n^2\right)\left(\frac{\pi^2}{8}QL_n\right)^2-\left(L_n+1-\frac{1}{\Omega_n^2}\right)\left(\frac{2}{\Omega_n^2}\right)\right]\frac{1}{\Omega_n}\cdot\frac{1}{\sin\left(\frac{\pi}{2}\Omega_n\right)}}{+\left[\sqrt{\left(L_n+1-\frac{1}{\Omega_n^2}\right)^2+\left(\left(\frac{1}{\Omega_n}-\Omega_n\right)\frac{\pi^2}{8}QL_n\right)^2}\right]^3}\right.$$
$$\left.\frac{\left(-\frac{\pi}{2}\frac{\cos\left(\frac{\pi}{2}\Omega_n\right)}{\sin^2\left(\frac{\pi}{2}\Omega_n\right)}\right)}{\sqrt{\left(L_n+1-\frac{1}{\Omega_n^2}\right)^2+\left(\left(\frac{1}{\Omega_n}-\Omega_n\right)\frac{\pi^2}{8}QL_n\right)^2}}\right]$$

$$K_v = \frac{2}{\pi}\frac{L_n}{\sin(\Omega_n\pi/2)}$$
$$\frac{1}{\sqrt{\left(L_n+1-\frac{1}{\Omega_n^2}\right)^2+\left(\left(\frac{1}{\Omega_n}-\Omega_n\right)\frac{\pi^2}{8}QL_n\frac{1}{\sin(\Omega_n\pi/2)}\right)^2}}. \quad (7)$$

In this case, there is no beat frequency dynamics and the circuit is essentially second-order.

C. *Unified Equivalent Circuit Model of* LLC

The small-signal models, shown in Figs. 6 and 16, can be combined to obtain a model that is valid both for $F_s \geq F_o$ and $F_s < F_o$. The unified equivalent circuit model is shown in Fig. 17. The expressions of L_e, R_e, and C_e are shown in (8). The expressions of K_v, G_v, K_d, and G_d are shown in (2) and (7)

$$L_e = \begin{cases}\left(1+\frac{1}{\Omega_n{}^2}\right)L_r & \text{for } \Omega_n = \frac{\Omega_s}{\Omega_o} \geq 1\\ \left(1+\frac{1}{\Omega_n{}^2}\right)L_r + \left(1-\Omega_n\right)L_m & \text{for } \Omega_n < 1\end{cases}$$

$$R_e = \begin{cases}\frac{L_e\left|X_{\text{eq}}\right|\left|\Omega_s-\Omega_o\right|}{R_{\text{eq}}}, & \text{for } \Omega_n \geq 1\\ 0, & \text{for } \Omega_n < 1\end{cases}$$

$$C_e = \frac{1}{L_e(\Omega_s-\Omega_o)^2}. \quad (8)$$

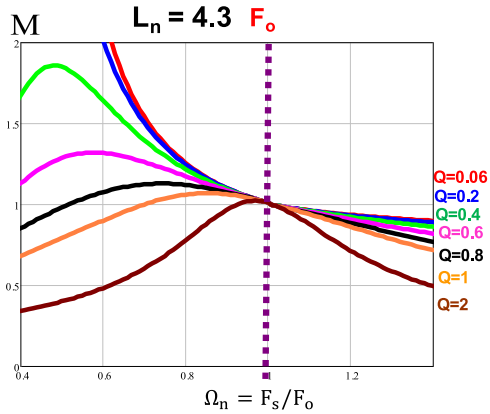

Fig. 18. Voltage conversion ratio of *LLC*.

III. Analysis and Predictions of the Proposed Equivalent Circuit Model

A. *Steady-State Voltage Conversion Ratio*

The steady-state voltage conversion ratio can be derived as in (9) and plotted in Fig. 18. When $F_s \geq F_o$, the dc gain is smaller than 1 and shows the characteristic of SRC. When $F_s < F_o$, the dc gain is greater than 1 and it shows the characteristic of parallel resonant converter. As will be shown in Section IV, since the mode change is considered when $F_s < F_o$, the voltage conversion ratio derived in this article is more accurate than traditional fundamental analysis [16]. However, as fundamental approximation is still used in this approach,

at low switching frequency, the gain curve starts to lose accuracy as there is more harmonics in the resonant variables. In this case, more precise steady-state analysis based on describing method and mode analysis can be employed to improve accuracy [29]–[33]

$$M = \frac{2nV_o}{V_g} = \frac{1}{\sin(\alpha/2)} \left\| \frac{j\Omega_n L_n}{j\Omega_n\left(L_n + 1 - \frac{1}{\Omega_n^2}\right) + \left(\frac{\pi^2}{8} Q \frac{1}{\sin(\Omega_n \pi/2)}\left(1-\Omega_n^2\right)\right) L_n \Omega_n} \right\|$$

$$\alpha = \begin{cases} \Omega_n \pi & \text{for } F_s < F_o \\ \pi & \text{for } F_s \geq F_o \end{cases}$$

$$L_n = \frac{L_m}{L_r}, Q = \frac{\sqrt{L_r/C_r}}{n^2 \cdot R_L}. \tag{9}$$

B. Small-Signal DC Gain and Beat Frequency Dynamics

With the help of Fig. 17, the three-dimensional (3-D) plot of control-to-output voltage transfer function can be plotted as Fig. 19. The small-signal dc gain and poles can be explained clearly using the proposed noncoupled equivalent circuit model shown in Fig. 17.

The dc gain of the control-to-output voltage transfer function can be derived easily. The dc gain can be related with the slope of the voltage conversion ratio curve by the relation shown in the following equation:

$$G_{\mathrm{DC}} = \frac{\partial V_o}{\partial \Omega_s} = \frac{V_g}{2n\Omega_o} \frac{\partial M}{\partial \Omega_s}. \tag{10}$$

When $\Omega_s > \Omega_o$, shown as the red curve in Fig. 19, the slope is negative and the starting phase in Fig. 19 is 180°. When $\Omega_s = \Omega_o$, shown as the blue curve, the slope is still negative due to the help of magnetizing inductor L_m. Therefore, the starting phase is still 180° and there is still certain amount of dc gain for the control-to-output transfer function. As a result, no canyon is observed for *LLC* resonant converter. This is an important difference compared with SRC, where the dc gain is zero at this point and there is a canyon in 3-D graph in Fig. 11, as also in [15]. From control point of view, SRC cannot be operated right at this point as it loses control. For *LLC* converter, with help of L_m, the gain of control-to-output voltage transfer function is not zero anymore. This means that the converter can be controlled operating right at this point. Actually, from efficiency point of view, it is preferred that *LLC* converter operating right at $F_s = F_o$ point. When $\Omega_s < \Omega_o$, shown as the black curve, the slope is still negative, and the circuit is still operated at ZVS region. This is also different compared with SRC, where the circuit operates at ZCS region when $\Omega_s < \Omega_o$.

The beat frequency dynamic performance of the circuit can also be well explained by the equivalent circuit. The components R_e, C_e, and L_e represent the beat frequency dynamics. The

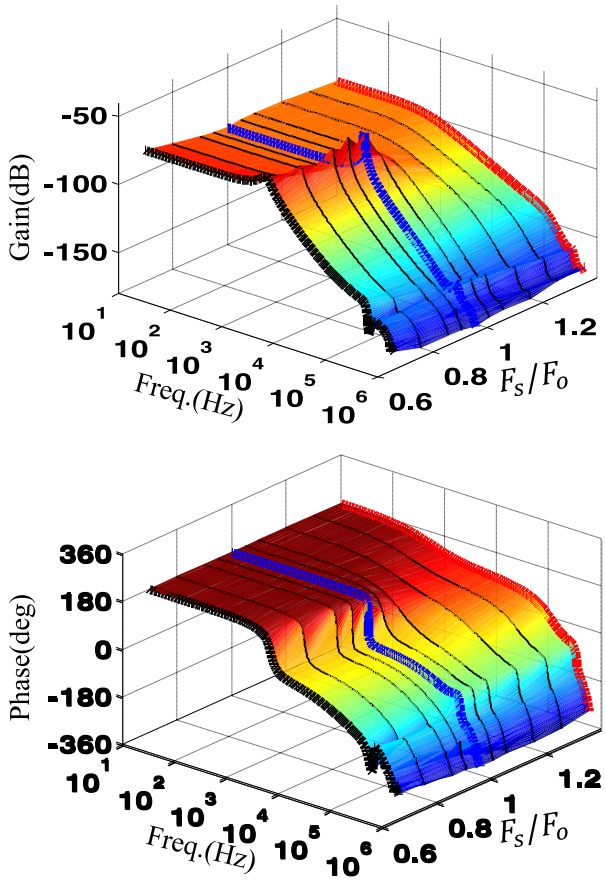

Fig. 19. 3-D Bode plots of control-to-output voltage transfer function.

equivalent inductor L_e is probably resonant with the equivalent output capacitor or the equivalent capacitor C_e, depending on the value of R_e.

When switching frequency F_s is much larger than resonant frequency F_o, R_e is large. L_e is resonant with C_e, which forms the beat frequency double pole. The output capacitor and load resistor form a single pole on the load side. In this case, the double pole position and its quality factor can be easily derived from Fig. 17, as in (11). Note that the position and quality factor of the beat frequency double pole are same as SRC. This is reasonable as when $F_s >> F_o$, *LLC* behaves like SRC and L_m does not participates in resonance; therefore, the effect of L_m on beat frequency double pole is very unobvious

$$\omega_p = |\Omega_s - \Omega_o|, Q_p = \frac{\left|\Omega_s L_r - \frac{1}{\Omega_s C_r}\right|}{R_{\mathrm{eq}}}. \tag{11}$$

When switching frequency F_s is larger than F_o but close to F_o, R_e is small. The double pole caused by L_e and C_e will be damped out and split, one moves to high frequency and the other one moves to low frequency. This low-frequency pole will combine with low-pass filter pole and forms a double pole. In other words, L_e resonates with equivalent output capacitor C_f and load resistance determines the damping factor of this double pole. In this case, the double pole position and its quality factor

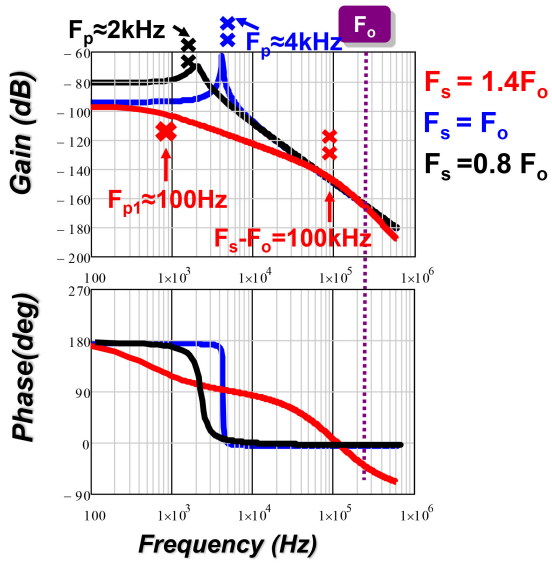

Fig. 20. 2-D Bode plots of control-to-output voltage transfer functions for *LLC*.

are shown as follows:

$$\omega_p = \sqrt{\frac{1}{L_e \frac{\pi^2}{8n^2} C_f}}, Q_p = \frac{8n}{\pi^2} R_L \sqrt{\frac{C_f}{L_e}}$$

$$L_e = \left(1 + \frac{1}{\Omega_n{}^2}\right) L_r. \tag{12}$$

When switching frequency F_s is below F_o, in this case, no beat frequency double pole exists. L_e resonates with equivalent output capacitor C_f and load resistance determines the damping factor of this double pole. However, in this case, L_e is modified by L_m according to (8) as there is a certain time period that L_m also participated in resonance. As a result, the double pole moves to a lower frequency with reduced quality factor. In this case, the double pole position and its quality factor are shown as follows:

$$\omega_p = \sqrt{\frac{1}{L_e \frac{\pi^2}{8n^2} C_f}}, Q_p = \frac{8n}{\pi^2} R_L \sqrt{\frac{C_f}{L_e}}$$

$$L_e = L_r \left(1 + \frac{1}{\Omega_n^2}\right) + L_m \left(1 - \Omega_n\right). \tag{13}$$

The following illustration example is provided to explain the beat frequency dynamics. When $F_s = 1.4F_o$, $R_e = 6.5\ \Omega$ is large, L_e resonates with C_e ($F_{\text{beat}} = 100$ kHz and $Q_{\text{beat}} = 0.6$). The 2-D Bode plot is shown as the red curve in Fig. 20; there is a beat frequency double pole at 100 kHz and a single pole at low frequency caused by the output filter. When $F_s = F_o$, $R_e = 0\ \Omega$ is very small. The beat frequency double pole is split. L_e resonates with output capacitor C_f. Shown as the blue curve in Fig. 20, the double pole formed by L_e and equivalent output capacitor, instead of beat frequency double pole, is observed. In this circumstance, the circuit is second-order instead of third-order. When $F_s = 0.8F_o$, the double pole reduces to around 3 kHz due to the increase of the equivalent resonant inductance. There is no beat frequency double pole in region $F_s < F_o$.

TABLE I
ANALYTICAL TRANSFER FUNCTIONS OF *LLC* RESONANT CONVERTER FOR $F_s \geq F_o$

$\frac{\hat{v}_o(s)}{\hat{\omega}_s(s)} = G_{DC} \frac{X_{eq}^2 + R_{eq}^2}{(s^2 L_e{}^2 + sL_e R_{eq} + X_{eq}^2)(1 + R_L C_f s) + R_{eq}(sL_e + R_{eq})}$ $G_{DC} = \frac{V_g}{2n} \frac{L_n}{\Omega_o \Omega_n} \frac{\left(\frac{1}{\Omega_n^2} - \Omega_n^2\right)\left(\frac{\pi^2}{8} Q L_n\right)^2 - \left(L_n + 1 - \frac{1}{\Omega_n^2}\right)\left(\frac{2}{\Omega_n^2}\right)}{\left[\sqrt{\left(L_n + 1 - \frac{1}{\Omega_n^2}\right)^2 + \left(\left(\frac{1}{\Omega_n} - \Omega_n\right)\frac{\pi^2}{8} Q L_n\right)^2}\right]^3}$ $L_e = (1 + \frac{\Omega_o{}^2}{\Omega_s{}^2}) L_r, R_{eq} = \frac{8}{\pi^2} n^2 R_L, X_{eq} = \Omega_s L_r - \frac{1}{\Omega_s C_r}, Q = \frac{\sqrt{L_r/C_r}}{n^2 \cdot R_L}, L_n = \frac{L_m}{L_r}$	(14)
$\frac{\hat{v}_o(s)}{\hat{v}_g(s)} = \frac{1}{2n} M_{st} \frac{R_{eq}{}^2 + X_{eq}^2 + L_e R_{eq} s}{(s^2 L_e{}^2 + sL_e R_{eq} + X_{eq}^2)(1 + R_L C_f s) + R_{eq}(sL_e + R_{eq})}$ $M_{st} = \left\| \frac{j\Omega_n L_n}{j\Omega_n \left(L_n + 1 - \frac{1}{\Omega_n^2}\right) + \frac{\pi^2}{8} Q(1 - \Omega_n^2) L_n} \right\|$	(15)
$Z_o(s) = R_L \frac{s^2 L_e{}^2 + sL_e R_{eq} + X_{eq}^2}{(s^2 L_e{}^2 + sL_e R_{eq} + X_{eq}^2)(1 + R_L C_f s) + R_{eq}(sL_e + R_{eq})}$	(16)
$Z_{in}(s) = \frac{\pi^2}{2} \frac{(s^2 L_e{}^2 + sL_e R_{eq} + X_{eq}^2)(1 + R_L C_f s) + R_{eq}(sL_e + R_{eq})}{s^2 L_e C_f R_L + sL_e + sC_f R_L \frac{R_{eq}{}^3}{R_{eq}{}^2 + X_{eq}^2} + R_{eq}}$	(17)

C. Analytical Expressions of Transfer Functions

Analytical expressions of transfer functions are of significant importance for design purpose. First of all, some popular design tools in industry, such as LTpowerCad from Analog Devices, are based on mathematical expressions of transfer functions. These design tools are much faster and simpler to use for designing of loop compensation, compared with real-time simulation. Second, in distributed power system, the input and output impedance plots are used for examination of the system stability. As an example, the input filter ahead of *LLC* resonant converter may cause the instability problem, depending on the magnitude of the output impedance of the filter and input impedance of *LLC* resonant converter [35]. Similarly, the output impedance is also needed to examine the stability if there is another dc–dc converter cascading following the output of *LLC* converter. Besides, the input-to-output transfer function is also used to examine the audio-susceptibility performance.

The analytical transfer functions are provided in Tables I and II for easy reference. These transfer functions are very helpful in designing the outer feedback compensator. For $F_s \geq F_o$, the transfer functions are generally third-order and can be reduced

TABLE II
ANALYTICAL TRANSFER FUNCTIONS OF *LLC* RESONANT CONVERTER FOR $F_s < F_o$

$\frac{\hat{v}_o(s)}{\hat{\omega}_s(s)} = G_{DC}\frac{1}{1+\frac{s}{Q_p\omega_p}+\left(\frac{s^2}{\omega_p{}^2}\right)}$ $Q_p = \frac{8n}{\pi^2}R_L\sqrt{\frac{C_f}{L_e}}$, $\omega_p = \sqrt{\frac{1}{L_e\frac{\pi^2}{8n^2}C_f}}$, $L_e = (1+\frac{\Omega_o{}^2}{\Omega_s{}^2})L_r + (1-\frac{\Omega_s}{\Omega_o})L_m$ *Expression of G_{DC} is shown at bottom of this page*	$(18)^2$
$\frac{\hat{v}_o(s)}{\hat{v}_g(s)} = \frac{1}{2n}M_{st}\frac{1}{1+\frac{s}{Q_p\omega_p}+\left(\frac{s^2}{\omega_p{}^2}\right)}$ $M_{st} = \frac{1}{\sin(\Omega_n\pi/2)}\left\|\frac{j\Omega_nL_n}{j\Omega_n\left(L_n+1-\frac{1}{\Omega_n^2}\right)+\frac{\pi^2}{8}Q(1-\Omega_n^2))\frac{1}{\sin(\Omega_n\pi/2)}L_n\Omega_n}\right\|$	(19)
$Z_o(s) = \frac{sL_e\frac{\pi^2}{8n^2}}{1+\frac{s}{Q_p\omega_p}+\left(\frac{s^2}{\omega_p{}^2}\right)}$	(20)
$Z_{in}(s) = \frac{\pi^2}{2}(sL_e + \frac{\frac{8n^2}{\pi^2}R_L}{R_LC_fs+1})$	(21)

to second-order when F_s is close to F_o. For $F_s < F_o$, the transfer functions are second-order.

IV. SIMULATION, EXPERIMENTAL VERIFICATIONS, AND DISCUSSION

A. Simulation Verifications

The SIMPLIS simulation tool is used to verify the voltage conversion ratio and small-signal analysis. Circuit parameters are shown as follows: $V_g = 400$ V, $L_r = 14\ \mu$H, $C_r = 30$ nF, $F_o = 250$ kHz, $C_f = 660\ \mu$F, $n = 4$, $R_L = 2.3\ \Omega$, the corresponding $Q = 0.6$. At resonant frequency, the output voltage is around 48 V with 1 kW full power.

Fig. 21 shows the comparison of the voltage conversion ratio using analytical equation (9) (solid lines) and simulation results

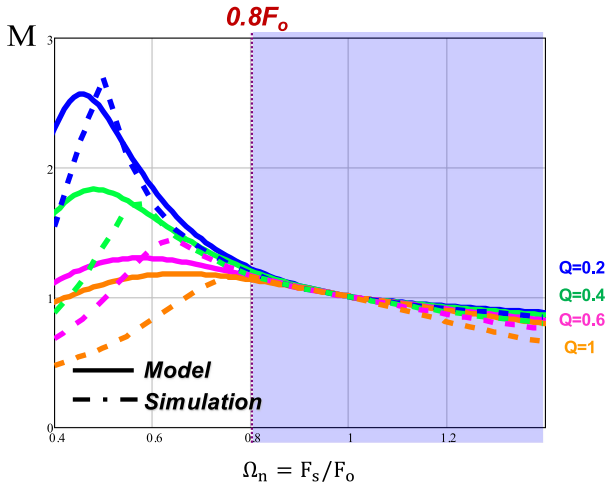

Fig. 21. SIMPLIS verification of voltage conversion ratio for *LLC* converter.

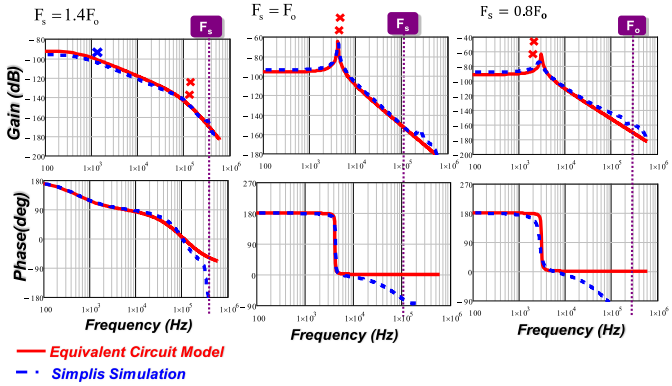

Fig. 22. SIMPLIS verification of control-to-output transfer function for $F_s = 1.4F_o$, $F_s = F_o$, and $F_s = 0.8F_o$.

(dashed lines) for quality factors equal to 0.2, 0.4, 0.6, and 1. The analytical solutions have good accuracy when $F_s \geq 0.8F_o$. However, as fundamental approximation is still used in this approach, at low switching frequency, the gain curve starts to lose accuracy as there is more harmonics in the resonant variables.

Fig. 22 shows SIMPLIS verification of control-to-output voltage transfer function for $F_s = 1.4F_o$, $F_s = F_o$, and $F_s = 0.8F_o$. In all three cases, the model matches very well with simulation results. As the previous analysis shows, when $F_s = 1.4F_o$, there is still a beat frequency double pole; when $F_s = F_o$, the beat frequency double pole splits and a new double pole formed by L_e and equivalent output capacitor C_f shows up; and when $F_s = 0.8F_o$, the double pole moves to a little lower frequency

$$G_{DC} = \frac{V_g}{2n}\frac{L_n}{\Omega_o}\frac{\left[\left(\frac{1}{\Omega_n^2}-\Omega_n^2\right)\left(\frac{\pi^2}{8}QL_n\right)^2-\left(L_n+1-\frac{1}{\Omega_n^2}\right)\left(\frac{2}{\Omega_n^2}\right)\right]\frac{1}{\Omega_n}\cdot\frac{1}{\sin\left(\frac{\pi}{2}\Omega_n\right)}+\left[\left(L_n+1-\frac{1}{\Omega_n^2}\right)^2+\left(\left(\frac{1}{\Omega_n}-\Omega_n\right)\frac{\pi^2}{8}QL_n\right)^2\right]\cdot\left(-\frac{\pi}{2}\frac{\cos\left(\frac{\pi}{2}\Omega_n\right)}{\sin\left(\frac{\pi}{2}\Omega_n\right)}\right)}{\left[\sqrt{\left(L_n+1-\frac{1}{\Omega_n^2}\right)^2+\left(\frac{1}{\Omega_n}-\Omega_n\frac{\pi^2}{8}QL_n\right)^2}\right]^3}$$

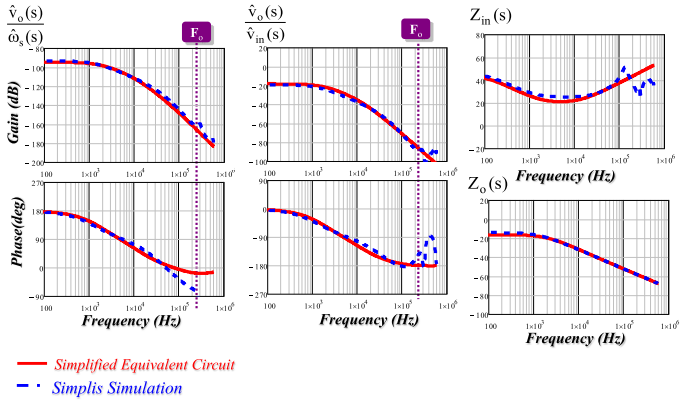

Fig. 23. SIMPLIS verification of small-signal equivalent circuit model for $F_s = 1.2F_o$.

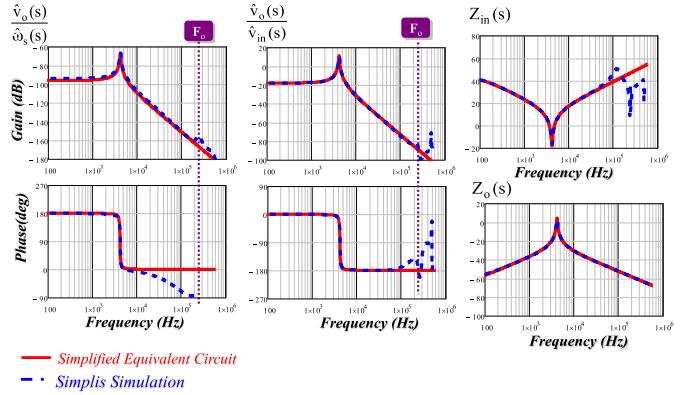

Fig. 24. SIMPLIS verification of small-signal equivalent circuit model for $F_s = F_o$.

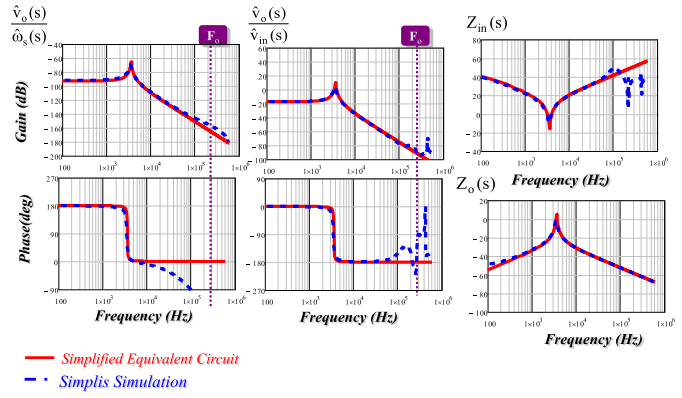

Fig. 25. SIMPLIS verification of small-signal equivalent circuit model for $F_s = 0.9F_o$.

as equivalent resonant inductor is increased to include the effect of magnetizing inductor.

To verify other transfer functions, Figs. 23–25 show the comparison of all the transfer functions between the equivalent circuit model and simulation results for $F_s = 1.2F_o$, $F_s = F_o$, and $F_s = 0.9F_o$, respectively. All the transfer functions match very well.

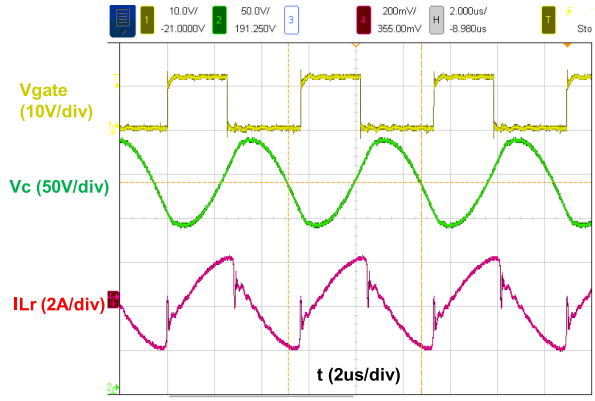

(a)

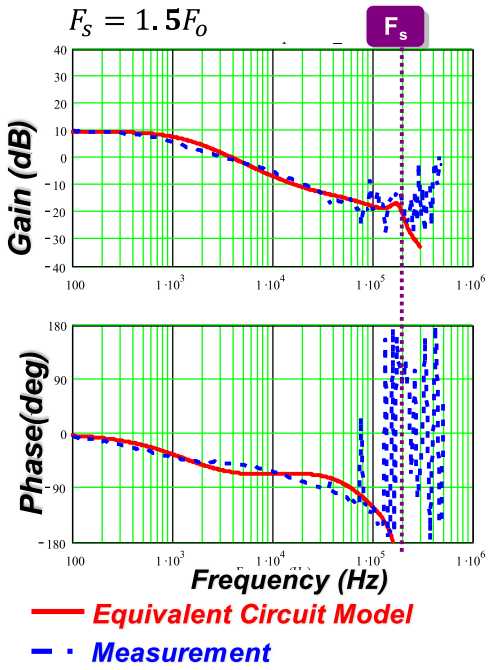

(b)

Fig. 26. (a) Experimental waveform of $F_s = 1.5F_o$. (b) Control-to-output voltage transfer function verification.

B. Experimental Verification

Experimental verification of the equivalent circuit model is also conducted based on the evaluation board of controller UCC25600 from Texas Instrument Incorporated [34]. The oscilloscope is used to capture the steady-state waveform, whereas the Bode plot machine Model 300 30-MHz Frequency Response Analyzer from Ridley Engineering is utilized to measure the transfer function. Traditional frequency modulation is utilized in UCC25600. Small-signal perturbation is injected through TP19 and TP21 in the evaluation board and control-to-output voltage transfer function is measured with U1 pin 4 and TP19 [34]. The major circuit parameters are as follows: $V_g = 320$–460 V, $V_o = 12$ V and is well controlled through closed feedback loop, $L_r = 55$ μH, $C_r = 24$ nF, $F_o = 115$ kHz, $C_o = 1660$ μF, $n = 17{:}1$, and $R_L = 1.2$ Ω. Fig. 26 shows the steady-state waveform and control-to-output voltage transfer function

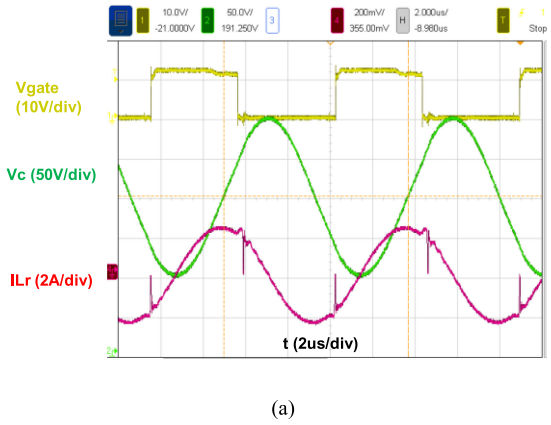

(a)

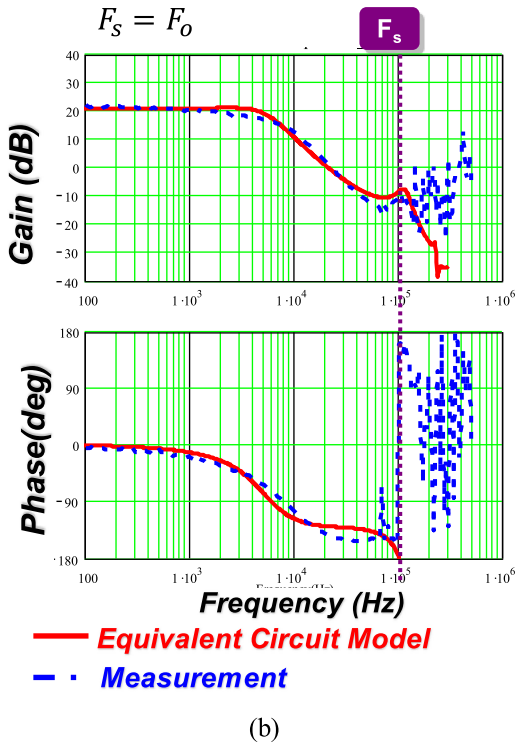

(b)

Fig. 27. (a) Experimental waveform of $F_s = F_o$. (b) Control-to-output voltage transfer function verification.

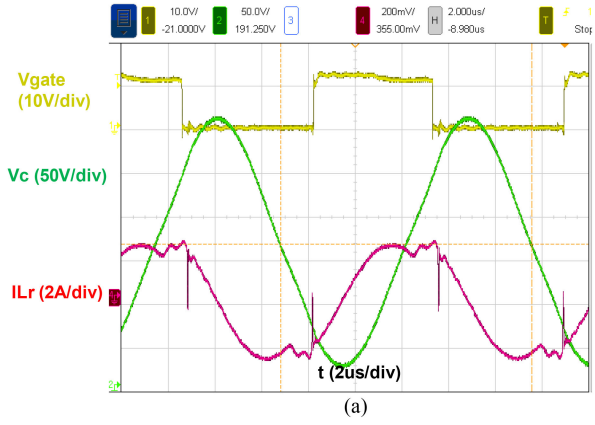

(a)

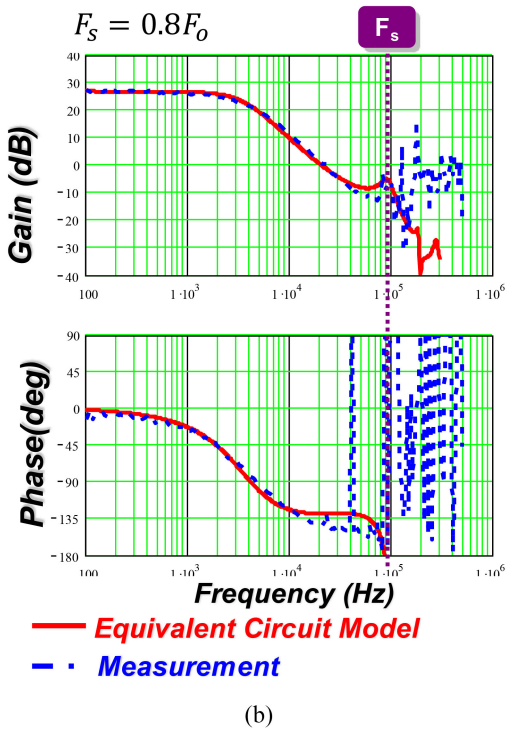

(b)

Fig. 28. (a) Experimental waveform of $F_s = 0.8F_o$. (b) Control-to-output voltage transfer function verification.

when $F_s = 176\,\text{kHz} = 1.5F_o$. The steady-state resonant current waveform shown in Fig. 26(a) confirms the circuit is running above resonant frequency. From Fig. 26(b), the small-signal behavior confirms that at low frequency it is a first-order system and additional phase delay exists due to high-frequency poles. Fig. 27 shows the steady-state waveform and control-to-output voltage transfer function when $F_s = 115\,\text{kHz} = F_o$. The steady-state resonant current waveform shown in Fig. 27(a), is almost sinusoidal, which confirms the circuit is running close to resonant frequency. From Fig. 27(b), the small-signal behavior confirms that in this case, a low-frequency double pole is formed so it is a second-order system instead of first order. Fig. 28 shows the steady-state waveform and control-to-output voltage transfer function when $F_s = 93\,\text{kHz} = 0.8\,F_o$. The steady-state resonant current waveform, shown in Fig. 28(a), confirms that the circuit is running below resonant frequency. From Fig. 28(b), the small-signal behavior confirms that in this case there is still a low-frequency double pole. As the model predicts, the double pole is at an even lower frequency compared with Fig. 27(b) due to participation of magnetizing inductor L_m in resonance. The measurement matches the prediction of the proposed model pretty well.

Digital control is more popular for *LLC* control due to the control complexity. The model is also verified on digital controlled *LLC* resonant converter from Delta Corporation. The experimental verification of control to output voltage is shown as Fig. 29. The circuit parameters of the hardware are as follows: $V_{\text{in}} = 50$ V, $L_r = 360$ nH, $L_m = 2.1$ μH, $C_r = 110$ nF, $C_f = 50$ μF, $n = 5{:}1$, $R_L = 1$ Ω, the corresponding $Q = 0.07$, $F_o = 800$ kHz, $F_s = 1.1$ MHz, and the delay term $T_d = 1$ μs.

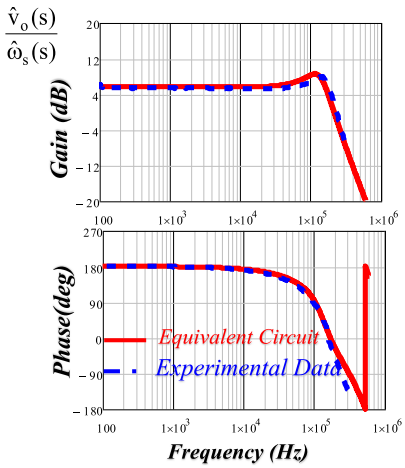

Fig. 29. Experimental verification of control-to-output transfer function on digitally controlled *LLC* converter.

From Fig. 29, the small-signal model matches very well with the experimental data. Note that due to the delay effect in digital control, the phase delay is more obvious. From Fig. 29 phase curve, we can see that there is almost 360° phase delay at 300 kHz. The excessive phase delay needs to be taken care of when designing the compensator, which usually limited the bandwidth of the circuit.

C. Discussion on Model Accuracy and Limitation

For $F_s \geq F_o$ region (above resonant), as shown in Fig. 2, L_m is clamped by either V_o or $-V_o$ and never participates in resonance; the equivalent circuit model of *LLC* is a direct extension from the equivalent circuit model of SRC [15], considering the loading effect of L_m branch. As a result, the poles and zeros of the transfer functions are same as SRC, whereas the gain of the transfer function is modified by L_m. This can be shown in (2), where the gain terms G_d, K_d, G_v, and K_v are affected by L_m. As shown in Fig. 19, the equivalent circuit model agrees with the simulation very well. However, as revealed in [28, Appendix B.1], Fig. 2 only represents the steady-state waveform under continuous conduction mode (CCM) for *LLC* resonant converter in this region. In fact, as load becomes lighter, the converter will work in to discontinuous conduction mode (DCM). In discontinuous mode, there is some "deadtime" where the resonant tank will be consisted with C_r and L_m in series with L_r. Therefore, the equivalent circuit model proposed is only valid for CCM. The models for DCM will be different as the basic operating principle changes. Fortunately, under normal condition, this is the major operating mode for *LLC* resonant converter working in this region. Only at very light load will the converter enter DCM.

For below resonant region, $F_s < F_o$, as shown in Fig. 7, the resonant tank changes at different time periods. In one of the time periods, the magnetizing inductor L_m participates in resonance. The equivalent resonant inductor concept is proposed to derive the model, as shown in Fig. 9 and (3). The model accuracy is good when F_s is close to F_o, for example, $F_s = 0.9F_o$. However, as the harmonics of switching frequency become more dominant, the fundamental approximation starts to lose accuracy and the model starts to break down when F_s is moving farther away from F_o. Generally speaking, for practical application operating in $F_s < 0.8F_o$ region, it is recommended that real circuit simulation is also implemented for an accurate small-signal model. Besides, the simulation shows that for some cases there is a right-half-plane zero in this region and this equivalent circuit model is not able to capture the dynamics related with the right-half-plane zero, therefore some phase discrepancy do exist when perturbation frequency is high. To improve the high-frequency accuracy, either a high-order equivalent circuit model or real-time simulation is required.

V. Summary

This article proposes an equivalent circuit model for *LLC* resonant converter. When $F_s \geq F_o$, L_m is clamped by the output voltage and *LLC* behaves very similar as SRC. As a result, the dynamic behavior is similar as SRC: when switching frequency is larger than resonant frequency, the beat frequency double pole shows up and the circuit is third order; when switching frequency is close to resonant frequency, beat frequency double pole disappears and a new double pole formed by equivalent inductor L_e and equivalent output capacitor C_f shows up. The circuit reduces to second-order. When $F_s < F_o$, L_m participates in resonance and the circuit is essentially a multiresonant structure. An approximated model is proposed where the equivalent resonant inductor is modified to include the effect of L_m. As a result, the double pole will move to a little lower frequency. For the first time, analytical solutions are provided for all the transfer functions that are very helpful for feedback design. Simulation and experimental results verify that the equivalent circuit model can well predict the dynamic behavior when switching frequency is below, close to, or above the resonant frequency.

Acknowledgment

The authors would like to express thanks to Delta Corporation for providing experimental data of digital controlled *LLC* converter.

References

[1] G. W. Wester and R. D. Middlebrook, "Low frequency characterization of switched dc-to-dc converters," in *Proc. IEEE Power Electron. Spec. Conf.*, 1972, pp. 9–20.
[2] R. D. Middlebrook and S. Cuk, "A general unified approach to modeling switching-converter power stages," in *Proc. IEEE Power Electron. Spec. Conf.*, 1976, pp. 18–34.
[3] R. Tymerski, V. Vorperian, F. C. Lee, and W. T. Baumann, "Nonlinear modeling of the PWM switch," *IEEE Trans. Power Electron.*, vol. 4, no. 2, pp. 225–233, Apr. 1989.
[4] V. Vorperian, "Simplified analysis of PWM converters using model of PWM switch. Continuous conduction mode," *IEEE Trans. Aerosp. Electron. Syst.*, vol. 26, no. 3, pp. 490–496, May 1990.
[5] J. Li and F. C. Lee, "New modeling approach and equivalent circuit representation for current mode control," *IEEE Trans. Power Electron.*, vol. 25, no. 5, pp. 1218–1230, May 2010.
[6] Y. Yan, F. C. Lee, and P. Mattavelli, "Unified three-terminal switch model for current mode controls," *IEEE Trans. Power Electron.*, vol. 27, no. 9, pp. 4060–4070, Sep. 2012.

[7] S. Tian, F. C. Lee, J. Li, Q. Li, and P. Liu, "A three-terminal switch model of constant on-time current mode with external ramp compensation," *IEEE Trans. Power Electron.*, vol. 31, no. 10, pp. 7311–7319, Oct. 2016.
[8] J. Li and F. C. Lee, "Modeling of V^2 current-mode control," *IEEE Trans. Circuits Syst. I, Reg. Papers*, vol. 57, no. 9, pp. 2552–2563, Sep. 2010.
[9] S. Tian, F. C. Lee, P. Mattavelli, K. Cheng, and Y. Yan, "Small-signal analysis and optimal design of external ramp for constant on-time V^2 control with multilayer ceramic caps," *IEEE Trans. Power Electron.*, vol. 29, no. 8, pp. 4450–4460, Aug. 2014.
[10] S. Tian, F. C. Lee, P. Mattavelli, and Y. Yan, "Small-signal analysis and optimal design of constant frequency V^2 control," *IEEE Trans. Power Electron.*, vol. 30, no. 3, pp. 1724–1733, Mar. 2015.
[11] S. Tian, F. C. Lee, Q. Li, and Y. Yan, "Unified equivalent circuit model and optimal design of V^2 controlled buck converters," *IEEE Trans. Power Electron.*, vol. 31, no. 2, pp. 1734–1744, Feb. 2016.
[12] V. Vorperian, "Approximate small-signal analysis of the series and the parallel resonant converters," *IEEE Trans. Power Electron.*, vol. 4, no. 1, pp. 15–24, Jan. 1989.
[13] E. X. Yang, F. C. Lee, and M. M. Jovanovic, "Small-signal modeling of power electronic circuits by extended describing function concept," in *Proc. Virginia Power Electron. Center Seminar*, 1991, pp. 167–178.
[14] S. Tian, F. C. Lee, Q. Li, and B. Li, "Small-signal equivalent model of series resonant converter," in *Proc. IEEE Energy Convers. Congr. Expo.*, 2015, pp. 172–179.
[15] S. Tian, F. C. Lee, and Q. Li, "A simplified equivalent circuit model of series resonant converter," *IEEE Trans. Power Electron.*, vol. 31, no. 5, pp. 3922–3931, May 2016.
[16] B. Yang, F. C. Lee, A. J. Zhang, and G. Huang, "LLC resonant converter for front end DC-DC conversion," in *Proc. 17th Annu. IEEE Appl. Power Electron. Conf. Expo.*, 2002, vol. 2, pp. 1108–1112.
[17] STMicroelectronics, "Reference design: High performance, L6599-based HB-LLC adapter with PFC for laptop computers," Application Notes AN2321, May 2007. [Online]. Available: http://www.mouser.com/catalog/specsheets/EVAL6599-90W.pdf
[18] C. Chang, E. Chang, C. Cheng, H. Cheng, and S. Lin, "Small signal modeling of LLC resonant converters based on extended describing function," in *Proc. Int. Symp. Comput. Consum. Control*, 2012, pp. 365–368.
[19] C. Buccella, C. Cecati, H. Latafat, P. Pepe, and K. Razi, "Linearization of LLC resonant converter model based on extended describing function concept," in *Proc. IEEE Int. Workshop Intell. Energy Syst.*, 2013, pp. 131–136.
[20] Z. Zahid, J. Lai, X. Huang, S. Madiwale, and J. Hou, "Damping impact on dynamic analysis of LLC resonant converter," in *Proc. IEEE Appl. Power Electron. Conf. Expo.*, 2014, pp. 2835–2841.
[21] C. Buccella, C. Cecati, H. Latafat, P. Pepe, and K. Razi, "Observer-based control of LLC DC/DC resonant converter using extended describing functions," *IEEE Trans. Power Electron.*, vol. 30, no. 10, pp. 5881–5891, Oct. 2015.
[22] B. Cheng, F. Musavi, and W. Dunford, "Novel small signal modeling and control of an LLC resonant converter," in *Proc. IEEE Appl. Power Electron. Conf. Expo.*, 2014, pp. 2828–2834.
[23] J. Stahl, T. Hieke, C. Oeder, and T. Duerbaum, "Small-signal analysis of the resonant LLC converter," in *Proc. IEEE Energy Convers. Congr. Expo. Asia*, 2013, pp. 25–30.
[24] B. Yang and F. C. Lee, "Small-signal analysis of LLC resonant converter," in *Proc. Center Power Electron. Syst. Seminar*, 2003, pp. 1–6.
[25] H. Huang, "Feedback loop design of an LLC resonant power converter," Texas Instruments Incorporated, Dallas, TX, USA, Appl. Rep. SLUA582A, Nov. 2010.
[26] S. Tian, "Equivalent circuit model of high frequency PWM and resonant converters," Ph.D. dissertation, Dept. Elect. Comput. Eng., Virginia Tech, Blacksburg, VA, USA, Aug. 2015.
[27] S. Tian, F. C. Lee, and Q. Li, "Equivalent circuit modeling of LLC resonant converter," in *Proc. IEEE Appl. Power Electron. Conf. Expo.*, 2016, pp. 1608–1615.
[28] B. Yang, "Topology inverstigation for front end DC/DC power conversion for distributed power system," Ph.D. dissertation, Dept. Elect. Comput. Eng., Virginia Tech., Blacksburg, VA, USA, Sep. 2003.
[29] J. Lazar and R. Martinelli, "Steady-state analysis of the LLC series resonant converter," in *Proc. IEEE Appl. Power Electron. Conf. Expo.*, 2001, pp. 728–735.
[30] T. Liu, Z. Zhou, A. Xiong, J. Zeng, and J. Ying, "A novel precise design method for LLC series resonant converter," in *Proc. IEEE Int. Telecommun. Energy Conf.*, Sep. 2006, pp. 1–6.
[31] M. P. Foster, C. R. Gould, A. J. Gilbert, D. A. Stone, and C. M. Bingham, "Analysis of CLL voltage-output resonant converters using describing functions," *IEEE Trans. Power Electron.*, vol. 23, no. 4, pp. 1772–1781, Jul. 2008.
[32] G. Ivensky, S. Bronshtein, and A. Abramovitz, "Approximate analysis of resonant LLC DC-DC converter," *IEEE Trans. Power Electron.*, vol. 26, no. 11, pp. 3274–3284, Nov. 2011.
[33] X. Fang, H. Hu, J. Shen, and I. Batarseh, "Operation mode analysis and peak gain approximation of the LLC resonant converter," *IEEE Trans. Power Electron.*, vol. 27, no. 4, pp. 1985–1995, Apr. 2012.
[34] UCC25600 Evaluation Board, Nov. 2018. [Online]. Available: http://www.ti.com/tool/UCC25600EVM
[35] R. Erickson and D. Maksimovic, *Fundamentals of Power Electronics*. New York, NY, USA: Springer, 2007.

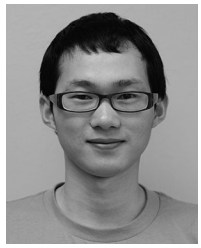

Shuilin Tian received the B.S. degree in electrical engineering from Zhejiang University, Hangzhou, China, in 2008, and the M.S. and Ph.D. degrees in electrical engineering from the Center for Power Electronics Systems, Virginia Tech, Blacksburg, VA, USA, in 2012 and 2015, respectively.

He is currently a Power uModule Design Manager with the Analog Devices, Inc., Santa Clara, CA, USA. He has authored/coauthored ten journal articles and 20 referred technical papers. His research interests include modeling, analysis, control of pulsewidth modulation converters and resonant converters, and integration and design of high-density, high-efficiency power uModule.

Fred C. Lee (Life Fellow, IEEE) received the B.S. degree in electrical engineering from the National Cheng Kung University, Tainan City, Taiwan, in 1968, and the M.S. and Ph.D. degrees in electrical engineering from Duke University, Durham, NC, USA, in 1972 and 1974, respectively.

He is currently a University Distinguished Professor Emeritus, Founder, and Director Emeritus of Center for Power Electronics Systems, a preeminent academic center in power electronics research at Virginia Tech, Blacksburg, VA, USA. He holds 89 US patents, and has authored/coauthored 310 journal articles and 740 refereed technical papers. His research interests include high-frequency power conversion, magnetics and electromagnetic interference, distributed power systems, renewable energy, power quality, high-density electronics packaging and integration, and modeling and control.

Qiang Li (Member, IEEE) received the B.S. and M.S. degrees from Zhejiang University, Hangzhou, China, in 2003 and 2006, respectively, and the Ph.D. degree from Virginia Tech, Blacksburg, VA, USA, in 2011.

He is currently an Associate Professor with the Center for Power Electronics Systems, Virginia Tech. His research interests include power management for distributed power systems, applications of WBG power devices, high-frequency power conversion and controls, magnetics and electromagnetic interference, high-density electronics packaging and integration, and renewable energy.

Dr. Li is a recipient of the First Place Prize Paper Award for 2016 in the IEEE TRANSACTIONS ON POWER ELECTRONICS and the 2017 National Science Foundation Career Award.